J. Fluid Mech. (2008), *vol.* 614, *pp.* 315–327.
doi:10.1017/S0022112008003285 Printed in the United Kingdom

Two-dimensional global low-frequency oscillations in a separating boundary-layer flow

UWE EHRENSTEIN[1] AND FRANÇOIS GALLAIRE[2]

[1]IRPHÉ UMR 6594, Aix-Marseille Université, CNRS, 49 Rue Joliot-Curie,
F-13384 Marseille Cedex 13, France
ehrenstein@irphe.univ.mrs.fr

[2]Laboratoire J. A. Dieudonné, Université de Nice-Sophia Antipolis, Parc Valrose,
F-06108 Nice Cedex 02, France
francois.gallaire@unice.fr

(Received 30 November 2007 and in revised form 20 June 2008)

A separated boundary-layer flow at the rear of a bump is considered. Two-dimensional equilibrium stationary states of the Navier–Stokes equations are determined using a nonlinear continuation procedure varying the bump height as well as the Reynolds number. A global instability analysis of the steady states is performed by computing two-dimensional temporal modes. The onset of instability is shown to be characterized by a family of modes with localized structures around the reattachment point becoming almost simultaneously unstable. The optimal perturbation analysis, by projecting the initial disturbance on the set of temporal eigenmodes, reveals that the non-normal modes are able to describe localized initial perturbations associated with the large transient energy growth. At larger time a global low-frequency oscillation is found, accompanied by a periodic regeneration of the flow perturbation inside the bubble, as the consequence of non-normal cancellation of modes. The initial condition provided by the optimal perturbation analysis is applied to Navier–Stokes time integration and is shown to trigger the nonlinear 'flapping' typical of separation bubbles. It is possible to follow the stationary equilibrium state on increasing the Reynolds number far beyond instability, ruling out for the present flow case the hypothesis of some authors that topological flow changes are responsible for the 'flapping'.

1. Introduction

Flow separation, which occurs in many industrial applications, is often synonymous with the loss of performance. Recirculation bubbles are likely to become unstable and the underlying mechanisms have received a lot of attention during the last two decades. The onset of three-dimensionality has been addressed by, among others, Kaiktsis, Karniadakis & Orszag (1991) and more recently by Williams & Baker (1997). It is now well established that the three-dimensional transverse instability is characterized by a global steady and weakly growing eigenmode (cf. Barkley, Gomes & Henderson 2002; Beaudoin *et al.* 2004; Gallaire, Marquillie & Ehrenstein 2007). While this longitudinal instability first takes place when the Reynolds number is increased, there is general evidence that laminar detached boundary layers are likely to undergo more violent two-dimensional low-frequency oscillations (Dovgal, Kozlov & Michalke 1994), known as 'flapping', which have been observed both in experiments and numerical simulations, whether the separation bubble is triggered by leading-edge geometries (Cherry, Hiller & Latour 1984)

or by adverse pressure gradients (Häggmark, Bakchinov & Alfredsson 2000; Pauley, Moin & Reynolds 1990).

The physical mechanisms at the origin of this type of instability which occurs above a critical Reynolds number are only partially understood. Recirculation bubbles appear to be very sensitive to external noise, thereby often concealing intrinsic instabilities (Kaiktsis, Karniadakis & Orszag 1996). The transitional energy growth associated with noise amplification has recently been investigated by Marquet *et al.* (2008). It seems however that typical frequencies for this amplifier dynamics are those of a convective Kelvin–Helmholtz instability of the shear layer and hence are too high to account for the large-scale 'flapping'. Frequencies associated with the possible transition from convective to absolute instability of local velocity profiles with a certain amount of reverse flow also appear to be higher than the typical frequencies associated with 'flapping' (cf. Hammond & Redekopp 1998; Rist & Maucher 2002). Convinced of the appearance of secondary recirculating flow regions at the rear of the main bubble, it has been conjectured (Dallmann *et al.* 1995; Theofilis, Hein & Dallmann 2000) that topological flow changes might be responsible for the overall instability behaviour. This possibility has been explored in Marquillie & Ehrenstein (2003) for a separated flow induced by a bump mounted on a flat plate but no clear-cut confirmation of topological flow changes could be given, in the absence of a basic state above criticality.

In this work we readdress the low-frequency oscillations for an elongated separation bubble induced by the bump geometry considered in Marquillie & Ehrenstein (2003). We focus on the two-dimensional global instability behaviour when the bump height is increased. The analysis combines a quasi-Newton approach to determine steady states beyond criticality and a numerical method suitable for computing two-dimensional temporal modes. Section 2 is devoted to the description of the numerical tools. In the present global approach, we assess the loss of stability by computing basic steady states for increasing bump heights in § 3. We show that steady states can be computed even far above the instability onset. An optimal perturbation analysis is performed in § 4. Optimal initial conditions are then used in the direct numerical simulation procedure and are shown to produce low-frequency 'flapping' described in § 5. Some conclusions are provided in § 6.

2. Numerical tools

The flow domain is $0 \leqslant x \leqslant L$, $\eta(x) \leqslant y \leqslant H$, with $\eta(x)$ the lower boundary containing the bump with height h. This bump shape with dimensionless height $h = 2$ has already been considered in Marquillie & Ehrenstein (2003) (cf. figure 1 for its geometry). An equivalent bump has been considered in wind tunnel experiments by Bernard *et al.* (2003): the shape has been optimized using Reynolds-averaged Navier–Stokes simulation results, for the adverse pressure at the rear of the bump to mimic that on the upper side of an airfoil at high angle of attack.

The height H of the upper boundary of the computational domain has been chosen large enough in order to recover uniform flow, the Navier–Stokes system being made dimensionless using the displacement thickness δ^* at inflow, where the Blasius profile is described, and the uniform free-stream flow velocity U_∞^*. The flow domain is transformed into $[0, L] \times [0, H]$ using, in the wall-normal direction, the transformation $\hat{y} = \gamma(y - \eta)$ with $\gamma = H/(H - \eta)$. The mapping

$$\bar{x} = \frac{2}{L}x - 1, \quad \hat{y} = \frac{Hs(1 + \bar{y})}{2s + H(1 - \bar{y})} \tag{2.1}$$

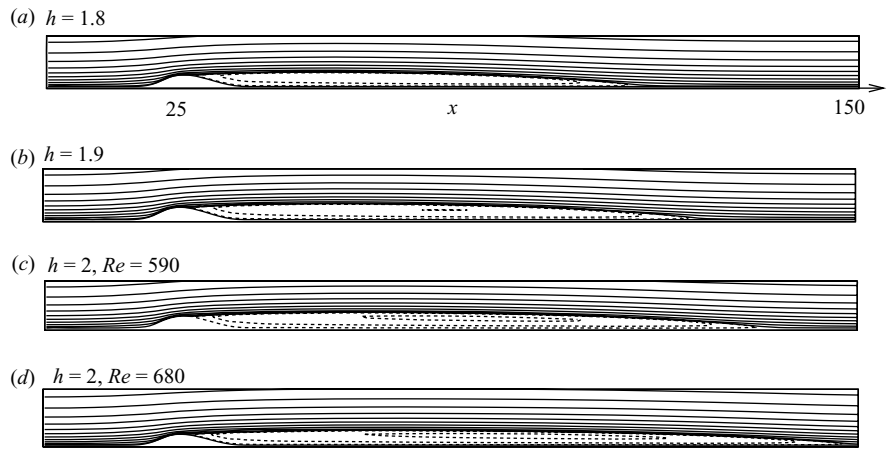

FIGURE 1. Streamlines of steady flow states obtained by continuation at (*a*) $Re = 590$, $h = 1.8$, (*b*) $Re = 590$, $h = 1.9$, (*c*) $Re = 590$, $h = 2$, (*d*) $Re = 680$, $h = 2$.

transforms the Cartesian domain into $[-1, 1] \times [-1, 1]$ and a Chebyshev–Chebyshev collocation discretization is used for the transformed system. In the wall-normal direction an algebraic mapping, used for instance by Joslin, Streett & Chang (1993) and Marquillie & Ehrenstein (2003), has been considered to account for the boundary-layer structure. The parameter s controls the grid-stretching and it has been assigned the value $s = H/10$. Here, we focus on nonlinear equilibrium states of the stationary Navier–Stokes system for increasing Reynolds number $Re = \delta^* U_\infty^*/\nu$ and hence the flow velocity $\boldsymbol{u} = (u, v)$ and pressure p are solutions of

$$\boldsymbol{f}(\boldsymbol{u}, p, Re) = [-(\boldsymbol{u}\cdot\nabla)\boldsymbol{u} - \nabla p + (1/Re)\nabla^2\boldsymbol{u}; \nabla\cdot\boldsymbol{u}] = \boldsymbol{0}. \tag{2.2}$$

Homogeneous Neumann boundary conditions for the flow field $\boldsymbol{u}$ are imposed at outflow $x = L$, whereas at $y = H$ uniform flow $\boldsymbol{u} = (1, 0)$ is prescribed and the no-slip condition applies on the wall boundary. At inflow the Blasius profile $(U(y), 0)$ is imposed. The Chebyshev–Chebyshev discretization is efficient in terms of precision versus grid-size. The problem of spurious pressure modes associated with a Chebyshev discretization in the square is overcome using extra conditions, by imposing the continuity of the normal derivative of the pressure at the corners and by eliminating the four modes for which the gradient vanishes due to the Chebyshev discretization (cf. Peyret 2002; Ehrenstein & Gallaire 2005).

A quasi-Newton method is used to compute the equilibrium states solution of (2.2), here the so-called *Broyden rank-one update procedure* making an affine approximation to the nonlinear function, which is justified close to an equilibrium state. In this procedure, only one complete QR-decomposition of the Jacobian matrix

$$\boldsymbol{A}(\boldsymbol{u}, Re) = D_{(\boldsymbol{u},p)}\boldsymbol{f}(\boldsymbol{u}, Re), \tag{2.3}$$

has to be performed when starting an iteration cycle: the operators for the subsequent linear systems are updated so that the corresponding QR decompositions can be computed with little extra-cost (cf. Stoer & Bulirsch 1992). The Reynolds number is added to the system as a parameter in an arclength continuation procedure. Once the solution has converged to a steady state $(\boldsymbol{u}_s, p_s)$, its stability is computed by considering two-dimensional temporal modes

$$\boldsymbol{u} = \hat{\boldsymbol{u}}(x, y)\mathrm{e}^{-\mathrm{i}\omega t}, \quad p = \hat{p}(x, y)\mathrm{e}^{-\mathrm{i}\omega t}. \tag{2.4}$$

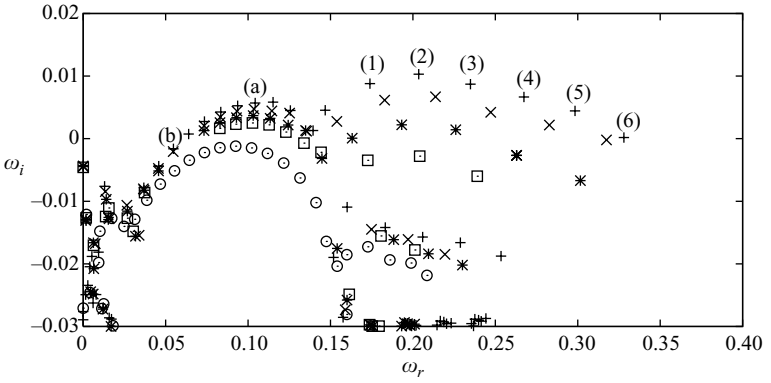

FIGURE 2. Eigenvalue spectrum at $Re = 590$ for several bump heights $h = 1.8$ (o), $h = 1.85$ ($\square$), $h = 1.9$ ($*$), $h = 1.95$ ($\times$), $h = 2$ ($+$). The modes labelled from (1) to (6) are depicted in figure 3 and modes (a), (b) in figure 4.

Taking into account in the Jacobian evaluated at a steady state $\boldsymbol{u}_s$ that the flow perturbation is zero at inflow, the modes are solutions of the generalized eigenvalue problem

$$-\mathrm{i}\omega \boldsymbol{B}\boldsymbol{q} = \boldsymbol{A}(\boldsymbol{u}_s, Re)\boldsymbol{q} \tag{2.5}$$

with $\boldsymbol{q} = (\hat{\boldsymbol{u}}, \hat{p})$ and $\boldsymbol{B}\boldsymbol{q} = (\hat{\boldsymbol{u}}, 0)$. The resulting large eigenvalue problem is solved using large-scale Krylov subspace projections together with the Arnoldi algorithm, similar to the approach used in Åkervik *et al.* (2007). In most computations the length of the computational domain is $L = 300$ and the height $H = 30$. This length of the box will be proved in § 4 to be large enough to minimize effects of the box size on the stability results. The modes are discretized using $Nx = 250$ collocation points in x and $Ny = 40$ collocation points in y, convergence being analysed in further detail in § 4. Finally a Krylov subspace with dimension $m = 1600$ has been considered. Contrary to the previous global mode analysis of our group (Ehrenstein & Gallaire 2005; Gallaire *et al.* 2007), no interpolation of the base state on the computational grid used for the global mode calculation is required here because the basic flow is directly calculated on the same grid.

3. Basic states and global instability analysis

In Marquillie & Ehrenstein (2003), for the same bump geometry with height $h = 2$ and using direct numerical simulation, the unsteadiness has been shown to appear for Reynolds numbers in the vicinity of $Re = 600$. Here we fix the Reynolds to $Re = 590$ and, taking advantage of our numerical continuation procedure, we compute steady states for increasing bump heights. The results are depicted in figure 1 and show that the recirculation length is very sensitive to bump height h. This may be physically understood since, the flow being accelerated on the ascending portion of a steeper bump, the boundary layer is more squeezed and therefore delivers more momentum into the shear layer when it detaches from the descending portion of the bump, thereby increasing the length of the detached bubble.

The sensitivity of the recirculation bubble with respect to the bump geometry is shown in the global stability results depicted in figure 2. For each computation, a Krylov subspace with dimension $m = 1600$ has been considered and roughly 400 converged eigenvalues (800 with the complex conjugates) are retrieved in the Arnoldi

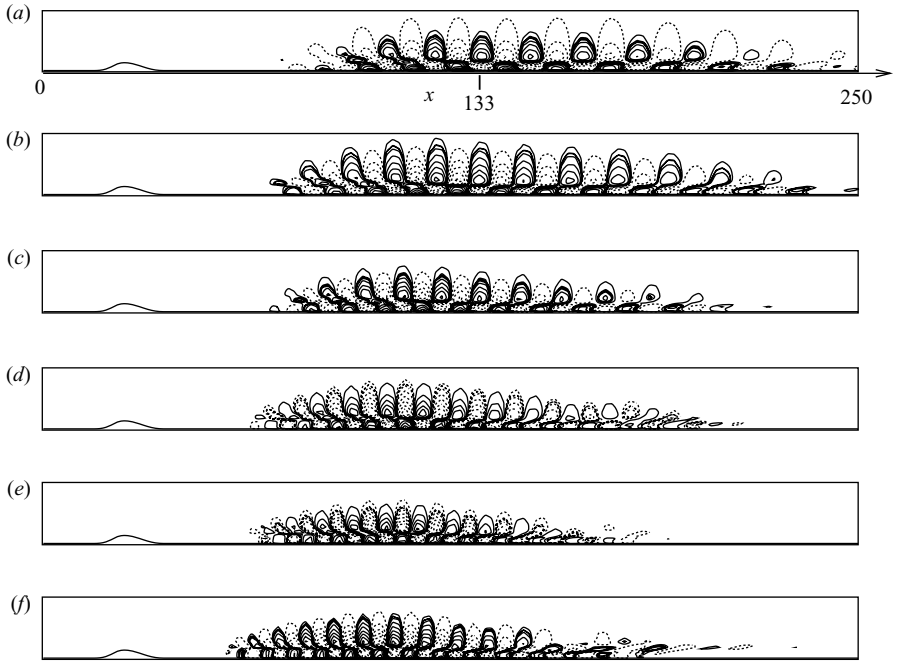

FIGURE 3. (*a–f*) Streamwise velocity components of eigenfunctions corresponding to eigenvalues labelled (1)–(6) in figure 2 for $Re = 590$ and $h = 2$.

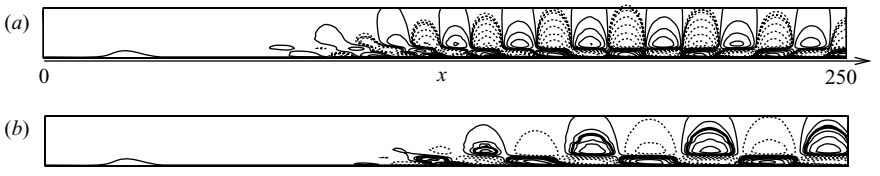

FIGURE 4. (*a*, *b*) Streamwise velocity components of eigenfunctions corresponding to eigenvalues labelled (*a*) and (*b*) in figure 2 for $Re = 590$ and $h = 2$ The reattachment point is located approximately at $x = 133$.

procedure. In figure 2 only the least stable and unstable parts of the spectra for increasing bump height h are shown to facilitate the comparison: while the flow is stable for $h = 1.8$, it becomes unstable for $h \sim 1.9$ and there are several unstable modes at $h = 2$. These modes, labelled from (1) to (6) in figure 2, become unstable almost simultaneously and the associated frequencies are equally spaced.

The localized modes labelled from (1) to (6) for $Re = 590$ and $h = 2$ in figure 2 are shown in figure 3. One observes that the modes originate approximately at the centre of the recirculation bubble and extend beyond the reattachment point, located approximately at $x = 133$. The modes have the same type of spatial structure, the upstream edge being shifted towards the bump as the frequency increases.

A second branch of weakly unstable 'convective' modes with lower frequencies is much less sensitive to the bump height variation. Typical structures of these modes are shown in figure 4: they are very reminiscent of the global modes associated with convective Tollmien–Schlichting instability which have been analysed for the flat plate boundary-layer flow by Ehrenstein & Gallaire (2005), Åkervik *et al.* (2008) and Alizard & Robinet (2007). The modes labelled (1)–(6) are not affected by the

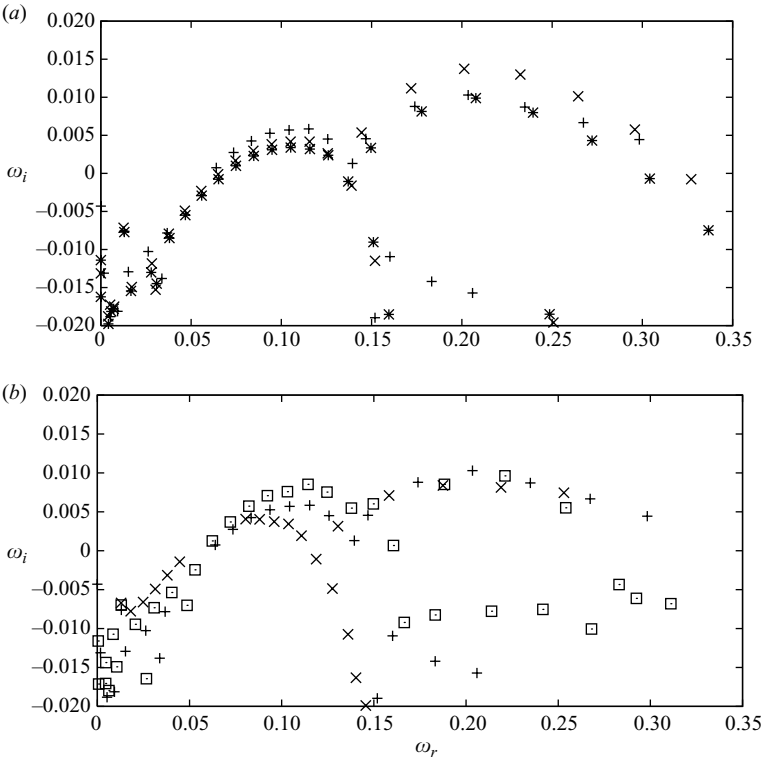

FIGURE 5. Dependence of the global spectrum on the domain size and resolution, for bump height $h = 2$, in comparison with, reference case $L = 300$ $H = 30$ $Nx \times Ny = 250 \times 40$, $Re = 590$ (+). (*a*) Variation of domain height H, for $L = 300$ ($Nx \times Ny = 250 \times 40$): $H = 40$, $Re = 590$ ($\times$), $H = 40$, $Re = 570$ ($*$). (*b*) Variation of domain length L for $H = 30$: $L = 400$, $Nx \times Ny = 250 \times 40$ ($\times$), $L = 300$, $Nx \times Ny = 200 \times 30$ for $Re = 590$ ($\square$).

homogeneous Neumann boundary condition considered here, the mode structure being vanishing at outflow. In Åkervik *et al.* (2008) it has been shown, comparing several boundary conditions, that this condition is also reliable for the Tollmien–Schlichting type temporal modes. While in the flat-plate boundary layer these modes are stable, the weak instability observed in the present case is most likely due to the influence of the reattachment region. Indeed, the structure of the weakly unstable mode labelled (*a*) in figure 2 is centred around the reattachment point where non-parallel effects are the strongest. Note that it has also been shown in Marquillie & Ehrenstein (2003) (cf. figure 7 therein) that in this Reynolds number range (for $h = 2$) the local profiles inside the recirculation bubble exhibit only very weak absolute damping rates, the flow being close to absolutely unstable. In contrast, the mode labelled (*b*) shown in figure 4 is located downstream in the weakly non-parallel flow region and it is seen to be stable.

Recall that these results have been obtained for a box length $L = 300$ and height $H = 30$, with $Nx = 250$ and $Ny = 40$. A convergence study has been conducted by increasing both the box length L and the domain height H. The corresponding eigenvalues are shown in figure 5 (again the least stable and unstable parts of the spectra are depicted). Fixing $L = 300$ the height has been increased and the results for $H = 40$ are shown in figure 5(*a*). An equivalent stretching parameter in the mapping

(2.1) has been considered, with $s = H/10$. The amplification rates for the modes with $\omega_r \geqslant 0.15$ are slightly increased, the frequencies being almost identical. The shift in the amplification rates may be compared with that produced by a weak shift in the Reynolds number, the results for $H = 40$ at $Re = 570$ being again close to the eigenvalues for $H = 30$ and $Re = 590$. For a domain height $H = 30$, the box length has been changed as well and the results are shown in figure 5(*b*). Although the exact modal frequencies do not converge to a set of points, the modes with $\omega_r \geqslant 0.15$ are now aligned on a single curve as shown in figure 5(*b*).

The computer memory requirements for the global stability analysis set a bound on the degree of discretization that can be considered and for this highly non-normal instability operator pointwise convergence of the spectrum can hardly be achieved (Trefethen & Embree 2005). The next section discusses that the global dynamics is due to the interaction of the modes rather than to individual eigenvalue locations. The family of unstable modes for $\omega_r \geqslant 0.15$ (corresponding to (1)–(6) in figure 2) will be seen to be of particular importance for the perturbation analysis to be performed.

In Marquillie & Ehrenstein (2003), the flow dynamics for the bump with $h = 2$ has been explored using direct numerical simulations. No steady states could be found for $Re > 600$, which is in accordance with the present global stability analysis. Given the present continuation procedure, basic states beyond criticality can easily be computed, one of which for $Re = 680$ (with bump $h = 2$) being shown in figure 1(*d*). Following Theofilis *et al.* (2000), it has been conjectured in Marquillie & Ehrenstein (2003) that topological flow changes may be responsible for the loss of stability. However, inspecting figure 1(*d*), it is seen that the recirculation length merely continues to increase without any particular change in the flow topology.

4. Optimal growth

When addressing the possibility of growth in a flow system, the notions of optimal initial condition and non-normality of the underlying operators are essential (Schmid & Henningson 2001). We are looking for initial disturbances $\boldsymbol{u}_0$ that maximize the energy at time t

$$G(t) = \max_{\boldsymbol{u}_0 \neq 0} \frac{||\boldsymbol{u}(t)||_E^2}{||\boldsymbol{u}_0||_E^2}, \tag{4.1}$$

with $||\boldsymbol{u}||_E^2 = \int \boldsymbol{u}^H \boldsymbol{u} \, \mathrm{d}x \, \mathrm{d}y$ the energy norm. A convenient form of this expression can be obtained by expanding the solution in terms of the generalized eigenmodes $\boldsymbol{u}(t) = \sum_{l=1}^{N} \kappa_l(t) \hat{\boldsymbol{u}}_l$ with $\hat{\boldsymbol{u}}_l$ a solution of (2.5). Hence the flow dynamics is described by

$$\frac{\mathrm{d}\boldsymbol{\kappa}}{\mathrm{d}t} = \boldsymbol{\Lambda}\boldsymbol{\kappa}, \quad \boldsymbol{\kappa}(0) = \boldsymbol{\kappa}_0, \tag{4.2}$$

where $\boldsymbol{\kappa}$ is the vector of expansion coefficients and $\boldsymbol{\Lambda}$ is a diagonal matrix whose elements are given by $\Lambda_l = -\mathrm{i}\omega_l$. The flow perturbation energy on this basis is $||\boldsymbol{u}||_E^2 = ||\boldsymbol{F} \exp(\boldsymbol{\Lambda} t)\boldsymbol{\kappa}_0||_2^2$, where $||\cdot||_2$ is the canonical Euclidean norm and $\boldsymbol{F}$ is the Cholesky factor of the Hermitian energy measure matrix $\boldsymbol{M}$ with entries $\boldsymbol{M}_{ij} = \int \hat{\boldsymbol{u}}_i^H \hat{\boldsymbol{u}}_j \, \mathrm{d}x \, \mathrm{d}y$ and hence $\boldsymbol{M} = \boldsymbol{F}^H \boldsymbol{F}$. The maximum growth expressed in the basis of eigenmodes reads

$$G(t) = ||\boldsymbol{F} \exp(\boldsymbol{\Lambda} t) \boldsymbol{F}^{-1}||_2^2 \tag{4.3}$$

and the largest growth at time t is given by the largest singular value of $\boldsymbol{F} \exp(\boldsymbol{\Lambda} t) \boldsymbol{F}^{-1}$ and the optimal initial condition is $\boldsymbol{\kappa}_0 = \boldsymbol{F}^{-1} z$ where z is the corresponding right

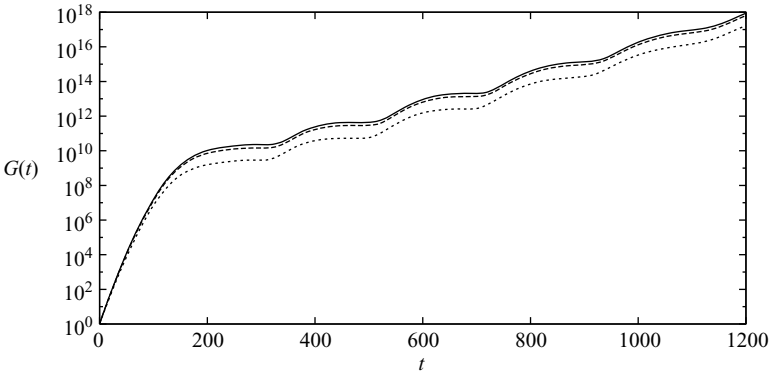

FIGURE 6. Envelope of maximum energy growth from initial condition, at $Re = 590$, $h = 2$ with three different truncations: $N = 406$ (solid line), $N = 300$ (broken line) and $N = 200$ (dotted line).

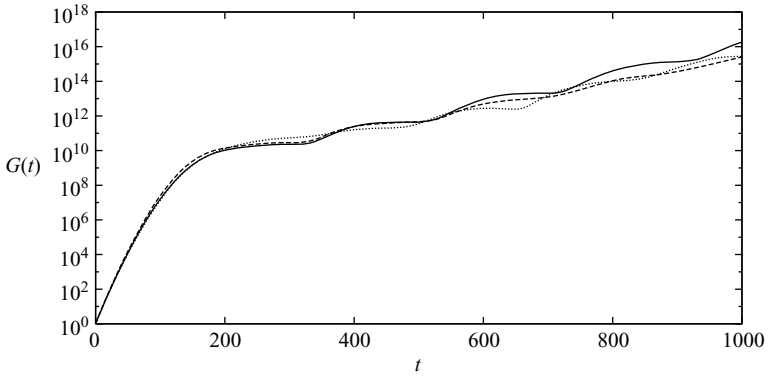

FIGURE 7. Convergence of the envelope of maximum energy growth from initial condition, at $Re = 590$ $h = 2$. Reference case $L = 300$, $Nx = 250$, $Ny = 40$ (solid line), $L = 400$, $Nx = 250$, $Ny = 40$ (dashed line) $L = 300$, $Nx = 200$, $Ny = 30$ (dotted line) ($H = 30$).

singular vector, hence providing the optimal initial flow condition $\boldsymbol{u}_0$ through the eigenmode expansion.

The optimal energy gains $G(t)$ are depicted in figure 6, for $Re = 590$. The large Krylov subspace procedure (with $m = 1600$) gives rise to a set of eigenvalues and its convergence in terms of optimal growth dynamics has been assessed. The result with $N = 406$ modes and the gain obtained for a much lower truncation at $N = 200$ (starting with the most unstable modes) are very close and differ by less than 1 %. The perturbation energy growth in time, starting with an optimal initial condition for any horizon $t > 200$, is the same as the envelope of the perturbation energy shown in figure 6. The optimal growth analysis has been performed for different box lengths and resolutions corresponding to the stability analysis shown in figure 5(*b*). The results are depicted in figure 7, and though the spectrum does not converge pointwise with resolution and domain length (cf. figure 5*b*), the resulting optimal transient growth is much more robust.

In all cases, a fast initial energy growth of a magnitude of almost 10^9 is observed as a consequence of streamwise non-normality (Chomaz 2005). This transient growth is followed by a global cycle with a period close to 200, the modulation being

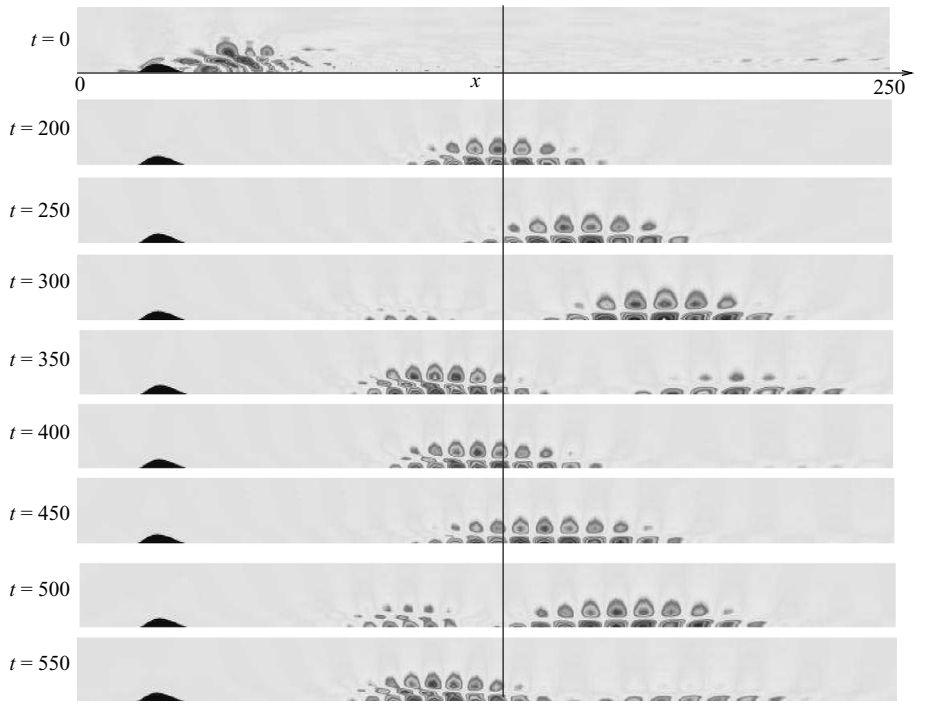

FIGURE 8. Streamwise velocity component of the perturbation for increasing time from top to bottom, starting with the optimal initial condition ($Re = 590$, $h = 2$). The vertical line shows the location of the reattachment point. The amplitude of the perturbation is normalized for each snapshot.

accompanied by a weak energy growth due to the amplification rates of the individual modes. Inspecting figure 2, one observes that the real parts of the unstable eigenvalues in the right half of the spectrum (the modes labelled from (1) to (6)) are about $\delta \approx 0.03$ apart and the structures of the corresponding eigenmodes are similar. The superposition of these modes as provided by the optimal perturbation analysis gives rise to cancelling and leads to the global period of $2\pi/\delta \approx 200$. Similar non-normal effects have also been described in a recent work on a separated flow in a cavity-like geometry by Åkervik *et al.* (2007) and in falling curtain flow by Schmid & Henningson (2002). This global beating is a new manifestation of streamwise non-normality characterized by a set of global eigenmodes bifurcating almost together, and displaying an analogous spatial structure. The flow above a wall-mounted bump, therefore, combines two typical features of non-normal operators: tremendous convective growth associated with a convective Kelvin–Helmholtz instability of the shear layer and low-frequency beating of weakly unstable modes.

To illustrate further the dynamical behaviour, the time evolution of the perturbation in the eigenmode system is depicted in figure 8, starting with the optimal initial condition which is mainly located in the vicinity of the rear part of the bump. The perturbation evolves along the plate as a localized wavepacket accompanied by an enormous increase of energy (in figure 8 the amplitude of the perturbation is renormalized for each snapshot) and at approximately $t = 250$ it is leaving the recirculation bubble. At the same time it reappears in the rear part of the bubble, which is visible at $t = 300$. The perturbation then evolves downstream (cf. structure at

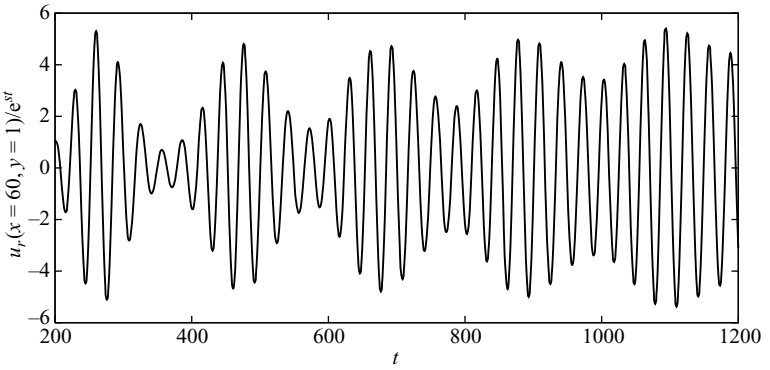

FIGURE 9. Local time trace of the velocity field at point ($x = 60$, $y = 1$) in the flow divided by e^{st} with $s = 0.0095$ close to the amplification factor of the most unstable mode (mode (2) in figure 2).

$t = 400$) before it reappears again in the bubble (cf. $t = 500$) and the cycle restarts. The modes responsible for the oscillating flow pattern are individually weakly unstable which leads to the overall growth shown in figure 6 (for $t > 200$).

Figure 9 displays a time record of the flow velocity near the centre of the recirculation bubble $x = 60$, $y = 1$, divided by e^{st} with $s = 0.0095$ and close to the most unstable mode (mode labelled (2) in figure 2). The carrier wave oscillates at a large frequency of approximately $\omega = 2\pi f \sim 0.2$, which corresponds to the frequency of the most unstable mode, and is modulated by the low-beating frequency.

5. Direct numerical simulation dynamics

Focusing on the relation between optimal energy growth and the low-frequency oscillations observed in previous investigations of the separation bubble, the optimal initial condition has been considered in the direct numerical simulation (DNS) procedure of the Navier–Stokes system used in Marquillie & Ehrenstein (2003).

The flow at $Re = 590$ is considered, which according to the present analysis is slightly supercritical. As shown in Marquillie & Ehrenstein (2003), at this Reynolds number it was however possible to converge by time marching to a steady state using the DNS procedure. Weak stabilization effects might be attributed to the influence of the outflow boundary of the shorter domain considered in the DNS (with $L = 200$), where a classical convection condition is applied. The streamwise direction is discretized using fourth-order finite differences with 1024 equidistant grid points. In the wall-normal y-direction the computational domain reaches the height $H = 80$ (with 97 Chebyshev-collocation points) for the solution to be uniform in the upstream region, a simple linear coordinate transform being employed. The gain in energy being expected to be close to 10^9, the optimal initial condition has been effected with a small maximum amplitude of 5×10^{-5} (however, this is above the residual noise of order of 10^{-6} in the time-marching towards the steady basic state $\boldsymbol{u}_b$). The energy of the perturbation $\boldsymbol{u}' = \boldsymbol{u} - \boldsymbol{u}_b$ has been integrated in the whole domain and the gain is depicted in figure 10. Up to $t = 200$ the energy growth follows the curve provided by the eigenmode system before the nonlinear saturation occurs. The integration has been pursued up to $t = 3000$ and the flow is seen to remain in a saturated nonlinear state. One may speculate whether the modulations visible in the global

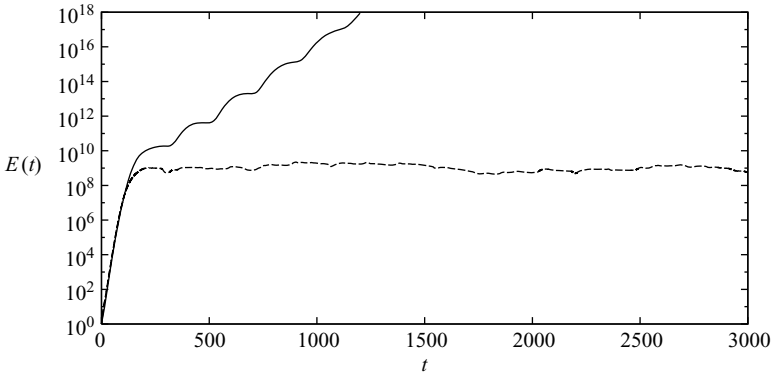

FIGURE 10. Global energy of $\boldsymbol{u} - \boldsymbol{u}_b$ in the time-integrated Navier–Stokes system at $Re = 590$, starting with optimal initial condition (broken line). Envelope of the eigenmode system is depicted as the solid line.

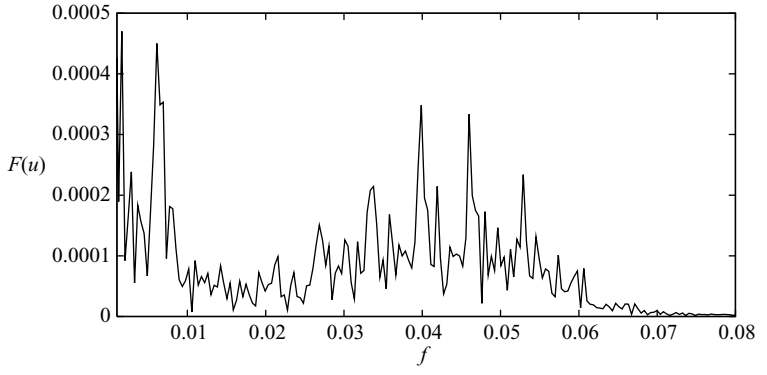

FIGURE 11. Power spectrum in time $500 \leqslant t \leqslant 3000$ of streamwise velocity component at $x = 60$, $y = 1$.

energy curve are somewhat reminiscent of the global oscillations in the linear gain prediction.

In this nonlinear stage, the global energy gain integrated over the whole domain is not the most appropriate measure. Focusing on the region inside the recirculation bubble at $x = 60$, $y = 1$, the Fourier transform of the time signal of the streamwise nonlinear perturbation flow velocity has been computed between time $t = 500$ and $t = 3000$. The resulting frequency spectrum shown in figure 11 displays a low-frequency peak $f \approx 0.005 \approx \delta/(2\Pi)$ very close to the 'beating' frequency in the eigenmodes system discussed in § 4. Of course, the power spectrum exhibits higher frequencies as well, which result from nonlinear interactions triggered by instabilities of Kelvin–Helmholtz type in the shear layer. Note that the spectrum measured by Marquillie & Ehrenstein (2003) (figure 5*b* therein) in their direct numerical simulation at $Re = 650$ is very similar to figure 11. This indicates that the low-frequency oscillation is a robust feature of the recirculation bubble under investigation: indeed, in Marquillie & Ehrenstein (2003), no particular initial perturbation has been prescribed and the self-sustained 'flapping' appeared spontaneously.

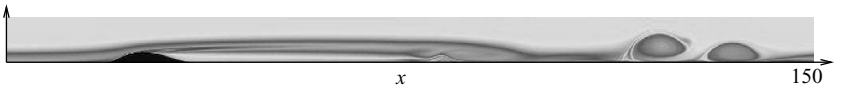

FIGURE 12. Instantaneous vorticity field from the DNS at $t = 1100$.

Figure 12 shows an instantaneous vorticity field illustrating the vortex-shedding behaviour resulting from the two-dimensional global oscillations.

6. Conclusion

In the aim of shedding new light on the phenomenon of global 'flapping' in separated wall-bounded flows, the two-dimensional flow over a bump, has been considered, by computing nonlinear states of the stationary Navier–Stokes system. When increasing the Reynolds number, no topological changes in the flow structure are detected.

The loss of stability of this separated flow is associated with a set of localized modes becoming simultaneously unstable. The upstream edges of the modes lie within the recirculation bubble and their tails extend beyond the reattachment point. While the structures of the modes are similar, their frequencies differ but are equally spaced. The dynamics resulting from the superposition of these non-normal modes give rise to a low-frequency beating due to alternate mode cancellations leading to a periodic regeneration of the resulting perturbation.

This has been confirmed by performing an optimal initial disturbance analysis, displaying the expected initial convective growth of disturbances in the shear layer followed by a global 'flapping' with frequency given by the frequency gap between the modes. The time-integration of the Navier–Stokes equations starting with the optimal initial condition leads to a nonlinear aperiodic flow with, however, clear evidence of the global low-frequency 'flapping' which is known to be a general feature of elongated recirculation bubbles. The underlying flow dynamics cannot be described by a single mode instability and the present global approach provides a new interpretation in terms of cancellation and regeneration of perturbation structures within a set of modes, leading to the large-scale beating behaviour.

Parts of the computations have been performed on the NEC-SX8 of the IDRIS, France. The authors would like to thank Matthieu Marquillie for providing the DNS code.

REFERENCES

ÅKERVIK, E., EHRENSTEIN, U., GALLAIRE, F. & HENNINGSON, D. S. 2008 Global two-dimensional stability measures of the flat plate boundary-layer flow. *Eur. J. Mech.* B/*Fluids* **27**, 501–513.

ÅKERVIK, E., HŒPFFNER, J., EHRENSTEIN, U. & HENNINGSON, D. S. 2007 Optimal growth, model reduction and control in a separated boundary-layer flow using global eigenmodes. *J. Fluid Mech.* **579**, 305–314.

ALIZARD, F. & ROBINET, J.-C. 2007 Spatially convective global modes in a boundary layer. *Phys. Fluids* **19**, 114105.

BARKLEY, D., GOMES, M. & HENDERSON, D. 2002 Three-dimensional instability in flow over a backward-facing step. *J. Fluid Mech.* **473**, 167–189.

BEAUDOIN, J.-F., CADOT, O., AIDER, J.-L. & WESFREID, J. 2004 Three-dimensional stationary flow over a backward-facing step. *Eur. J. Mech.* B/*Fluids* **23**, 147–155.

BERNARD, A., FOUCAUT, J. M., DUPONT, P. & STANISLAS, M. 2003 Decelerating boundary layer: a new scaling and mixing length model. *AIAA J.* **41**, 248–255.

Cherry, N. J., Hiller, R. & Latour, M. P. 1984 Unsteady measurements in a separating and reattaching flow. *J. Fluid Mech.* **144**, 13–46.

Chomaz, J.-M. 2005 Global instabilities in spatially developing flows: non-normality and nonlinearity. *Annu. Rev. Fluid Mech.* **37**, 357–392.

Dallmann, U., Herberg, Th., Gebing, H., Su, W.-H. & Zhang, H.-Q. 1995 Flow field diagnostics: topological flow changes and spatio-temporal flow structure. *AIAA Paper* 95-791.

Dovgal, A. V., Kozlov, V. V. & Michalke, A. 1994 Laminar boundary layer separation: instability and associated phenomena. *Prog. Aerospace Sci.* **30**, 61–94.

Ehrenstein, U. & Gallaire, F. 2005 On two-dimensional temporal modes in spatially evolving open flows: the flat-plate boundary layer. *J. Fluid Mech.* **536**, 209–218.

Gallaire, F., Marquillie, M. & Ehrenstein, U. 2007 Three-dimensional transverse instabilities in detached boundary-layers. *J. Fluid Mech.* **571**, 221–233.

Häggmark, C. P., Bakchinov, A. A. & Alfredsson, P. H. 2000 Experiments on a two-dimensional laminar separation bubble. *Phi. Trans. R. Soc. Lond.* A. **358**, 3193–3205.

Hammond, D. A. & Redekopp, L. G. 1998 Local and global instability properties of separation bubbles. *Eur. J. Mech.* B/*Fluids* **17**, 145–164.

Joslin, R. D., Streett, C. L. & Chang, C.-L. 1993 Spatial direct numerical simulation of boundary-layer transition mechanisms: validation of pse theory. *Theoret. Comput. Fluid Dyn.* **4**, 271–288.

Kaiktsis, L., Karniadakis, G. E. & Orszag, S. A. 1991 Onset of three-dimensionality, equilibria and early transition in flow over a backward-facing step. *J. Fluid Mech.* **231**, 501–528.

Kaiktsis, L., Karniadakis, G. E. & Orszag, S. A. 1996 Unsteadiness and convective instabilities in two-dimensional flow over a backward-facing step. *J. Fluid Mech.* **321**, 157–187.

Marquet, O., Sipp, D., Chomaz, J.-M. & Jacquin, L. 2008 Amplifier and resonator dynamics of a low-Reynolds-number recirculation bubble in a global framework. *J. Fluid Mech.* **605**, 429–443.

Marquillie, M. & Ehrenstein, U. 2003 On the onset of nonlinear oscillations in a separating boundary-layer flow. *J. Fluid Mech.* **490**, 169–188.

Pauley, L. L., Moin, P. & Reynolds, W. C. 1990 The structure of two-dimensional separation. *J. Fluid Mech.* **220**, 397–411.

Peyret, R. 2002 *Spectral Methods for Incompressible Flows*. Springer.

Rist, U. & Maucher, U. 2002 Investigations of time-growing instabilities in laminar separation bubbles. *Eur. J. Mech.* B/*Fluids* **21**, 495–509.

Schmid, P. J. & Henningson, D. S. 2001 *Stability and Transition in Shear Flows*. Springer.

Schmid, P. J. & Henningson, D. S. 2002 On the stability of a falling liquid curtain. *J. Fluid Mech.* **463**, 163–171.

Stoer, J. & Bulirsch, R. 1992 *Introduction to Numerical Analysis*. Springer.

Theofilis, V., Hein, S. & Dallmann, U. 2000 On the origins of unsteadiness and three-dimensionality in a laminar separation bubble. *Phil. Trans. R. Soc. Lond.* A **358**, 3229–3246.

Trefethen, N. & Embree, M. 2005 *Spectra and Pseudospectra; The Behaviour of Nonnormal Matrices and Operators*. Princeton University Press.

Williams, P. T. & Baker, A. J. 1997 Numerical simulations of laminar flow over a 3d backward-facing step. *Intl J. Numer. Meth. Fluids* **24**, 1159–1183.